NPL
National Physical Laboratory

Report

NPL REPORT IR 3

EXPERIMENTAL SET-UP FOR ALANINE DOSIMETRY IN PROTONS BELOW 18 MEV

Hugo Palmans, Jozef Dobrovodský, Norman Durný, Claire Gouldstone, Peter Kováč, Jozef Martinkovič, Matuš Mozolík, Márius Pavlovič, Karen Rosser, Peter Sharpe and Ondrej Szöllős

NOT RESTRICTED

DECEMBER 2007

National Physical Laboratory | Hampton Road | Teddington | Middlesex | United Kingdom | TW11 0LW
Switchboard 020 8977 3222 | **NPL Helpline** 020 8943 6880 | **Fax** 020 8614 0446 | **www.npl.co.uk**

Department for **Innovation, Universities** & **Skills**

EXPERIMENTAL SET-UP FOR ALANINE DOSIMETRY IN PROTONS BELOW 18 MEV

Hugo Palmans[1], Jozef Dobrovodský[2], Norman Durný[2], Claire Gouldstone[1], Peter Kováč[3], Jozef Martinkovič[2], Matuš Mozolík[3], Márius Pavlovič[4], Karen Rosser[5], Peter Sharpe[1] and Ondrej Szöllős[3]

[1]Radiation Dosimetry Team, National Physical Laboratory

[2]Slovak Institute of Metrology, Bratislava, Slovakia

[3]Biont, Bratislava, Slovakia

[4]Slovak Technical University, Bratislava, Slovakia

[5]Royal Marsden Hospital, Sutton, UK

ABSTRACT

An experimental set-up was created at the existing Biont 18 MeV proton beam line for measuring the response of alanine to protons in the energy region below 18 MeV. Extensive Monte Carlo simulations were performed in support of the design and characterisation of the beam line as well as for the interpretation of the experimental data. An experiment was performed comparing alanine, radiochromic film and a Markus ionization chamber. The experiments demonstrated that a stable beam of sufficiently low intensity for dosimetry could be produced. With the present set-up, accurate relative measurements using a stack of alanine pellets and accurate absolute calibration of one or more alanine pellets by directly placing them in front of a Markus chamber could be performed, provided the spectral characteristics and stability of the beam steering are improved. Based on the experience and Monte Carlo simulations, suggestions for such improvements are made.

ISSN 1754-2952

National Physical Laboratory
Hampton Road, Teddington, Middlesex, TW11 0LW

Approved on behalf of the Managing Director, NPL
by Dr Martyn Sene, Director, Division Quality of Life

CONTENTS

1. INTRODUCTION

Up to now, the treatment of eye melanoma has been the most important application of proton therapy. For the treatment of these lesions proton beams with a range smaller than 3.5 cm in water are used. This corresponds to energies below 65 MeV. This treatment technique takes advantage of the depth dose distribution of a proton beam exhibiting a high dose peak at the end of the proton range, the Bragg peak, beyond which the dose falls rapidly to zero.

Crystalline alanine has been used since the 1960's for dosimetry of light and heavy ions and has gained renewed attention as a potential absolute dosimeter recently. Alanine is usually used in powder form and mixed with a binding agent such as paraffin or cellulose in order to shape it into small dosimeters that can be easily handled. Alanine is an amino acid and it forms a stable radical when ionised by radiation. Dosimetry with alanine is based on the measurement of the amount of radiation-induced radicals formed by means of the electron spin resonance (ESR) technique. This is achieved by applying a magnetic field and then supplying electromagnetic energy in the microwave frequency range, which induces magnetic dipole transitions to the spin states of the unpaired electron in the radical. Quantification of the absorbed microwave energy around the resonance frequency yields the ESR spectrum, the amplitude of which is a measure of the amount of radicals formed. Advantages of the alanine dosimeter are that the signal is preserved after read-out and exhibits long time stability, the composition is nearly tissue equivalent and the dose response is linear over a wide dose range. Disadvantages are that the sensitivity of the technique is rather low such that the required doses are an order of magnitude larger than usually applied in a radiotherapy treatment fraction and that the ESR technique is quite elaborous.

The response of alanine is known to be dependent on the type of radiation. To this end the relative effectiveness (RE) for protons is introduced, defined as the ratio of the detector signals for the same amounts of absorbed dose by protons and by ^{60}Co gamma radiation. Various authors have measured the RE of alanine for protons by comparing its response with that for an ionisation chamber (Fattibene et al., 1996, Onori et al. 1996, 1997, Cuttone et al. 1999, Bartolotta et al. 1999). Bradshaw et al. (1962), Ebert et al. (1965), Hansen and Olsen (1985), Olsen and Hansen (1990) and Fattibene et al. (2002) derived the alanine RE from total absorption of a measured number of protons with a known amount of energy. In the most recent of these experiments (Fattibene et al. 2002), total absorption experiments in proton beams with energies of 6 MeV and lower showed a decrease in RE to 60%.

Palmans (2003) reviewed these experimental data and proposed sigmoid curve fittings of the form:

$$\mathrm{RE}(E_{eff}) = \mathrm{RE}_0 + \frac{\Delta\mathrm{RE}}{1 + e^{-C\cdot(\log(E_{eff})-\log(E_m))}} \qquad (1)$$

where RE_0, ΔRE, C and E_m are parameters and their values for the different fits have been given in table 1 and represented in figure 1 together with the data from the literature discussed above. In addition, data from Olsen and Hansen (1990) were added, which were extracted from a graph presented by Bassler (2006).

Table 1. Parameters of the sigmoid curves fitted to experimental data from the literature (reproduced from Palmans 2003).

Curve no	ΔRE	$\log(E_m)$	C	RE_0
1	1.0000	-0.2238	1.8322	0.0000
1’	1.0000	-0.2165	1.9095	0.0000
2	0.4000	0.6219	2.8921	0.6000
3	0.3819	0.9673	6.7193	0.6181

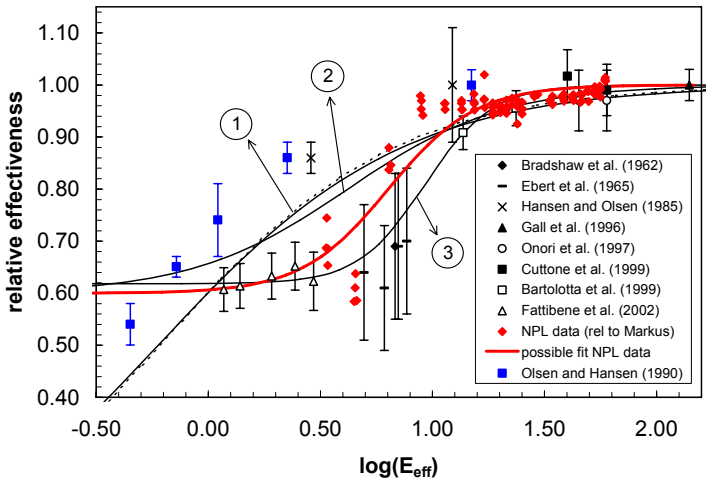

Figure 1. Experimental values of the relative effectiveness of alanine as a function of effective proton energy (data points) and sigmoid fits with equation (1) and the parameters from table 1 (curves). The data were reproduced from Palmans (2003) with addition of data points from Olsen and Hansen (1990) and preliminary results obtained in CCO.

Waligorski et al. (1989) compared experimental data with results of calculations based on track structure theory. Their results indicate the same qualitative decrease of alanine response with decreasing energy (or increasing LET). The theoretical values they found are in general higher than the experimental values, but lower than the results of Bartolotta et al. (1999).

Alanine has also been investigated as a relative detector and several authors have investigated its suitability for depth dose measurements compared to other detectors (Nichiporov et al. 1995, Fattibene et al. 1996, Gall et al. 1996, Onori et al. 1996, 1997 and Bartolotta et al. 1999) in general with satisfying agreement with plane-parallel ionisation chambers.

NPL's therapy level alanine dosimetry service has been described by Sharpe et al. (1996) and Sharpe and Sephton (2000). The alanine pellets consist of a mixture of 90% alanine and 10% paraffin wax. They have a diameter of 5 mm and a nominal thickness of 0.5 mm or 2.5 mm. The readout is performed with a Bruker ESP 300 X-band 9” magnet. Every batch of pellets is calibrated separately against NPL’s primary standard for absorbed dose to water in ^{60}Co based on graphite calorimetry.

Information on the response of NPL's alanine system in proton beam was obtained at the Clatterbridge Centre of Oncology (CCO) by performing absolute comparison against the dose measured by a Markus ionisation chamber and by relative depth dose measurement using a stack of alanine pellets in a PMMA phantom. The preliminary results from these measurements are shown in figure 1 together with a possible fit, assuming a saturation level of 60% at low-energy (Palmans et al. 2006). The main problem with these results is that in the energy region below 10 MeV, where the reduction of RE becomes substantial, the proton spectrum is very wide due to energy straggling and the assignment of a single energy to the data point is not accurate.

This work aims to create a beam line able to measure the response of alanine to protons in the energy region below 18 MeV with a better energy resolution. To this end the existing beam line at Biont needs to be modified in order to reduce the beam current reaching the dosimetry set-up, to create a homogeneous beam by collimation and a double scatterer and to provide some beam stabilising mechanism. In this report an overview is given of Monte Carlo simulations performed in support of the design and studying the properties of the beam line and of the preliminary experience with the beam line leading to proposals for improvement.

2. METHOD

2.1. Experimental set-up

2.1.1. Beam line

Biont operates an IBA Cyclone® 18/9 isochronous cyclotron which produces protons of 18 MeV and deuterons of 9 MeV. The proton beam current varies between about 1 μA and 100 μA, much higher than typical currents for radiotherapy (order 1 nA). The ion source is a PIG internal type. The hill and valley gaps are respectively 3 cm and 67 cm resulting in a magnetic field variation between 1.9 T and 0.35 T. The injection radius is 3 cm, the pole diameter 108 cm and the extraction radius 48 cm. The RF amplitude is 32 kV (peak to ground) with a frequency of 42 MHz. The cyclotron actually accelerates negatively charged ions (H- for producing a proton beam) and the beam is extracted by a 100% efficiency carbon stripper foil.

The main characteristics of the beam line used for the experiments in this report are described schematically in figure 2. The primary collimator was inserted 40 cm into the beam pipe (more or less the deepest possible for being able to tighten it into the pipe after positioning). This allows a gap of 16 cm between the steering magnet and the collimator. The 50 μm Titanium exit window was replaced with a double aluminium foil (25 μm each) between which a flow of helium gas provided cooling. The final collimators were mounted on the existing mounting bars normally used for the beam dump.

From the beam transport point of view, the beam-line represents a simple ion-optical system consisting of a drift space, quadrupole doublet and drift space. The steering magnet at the beginning of the beam-line is basically used to align the extracted beam with the axis of the extraction channel and its focusing/defocusing action can be neglected.

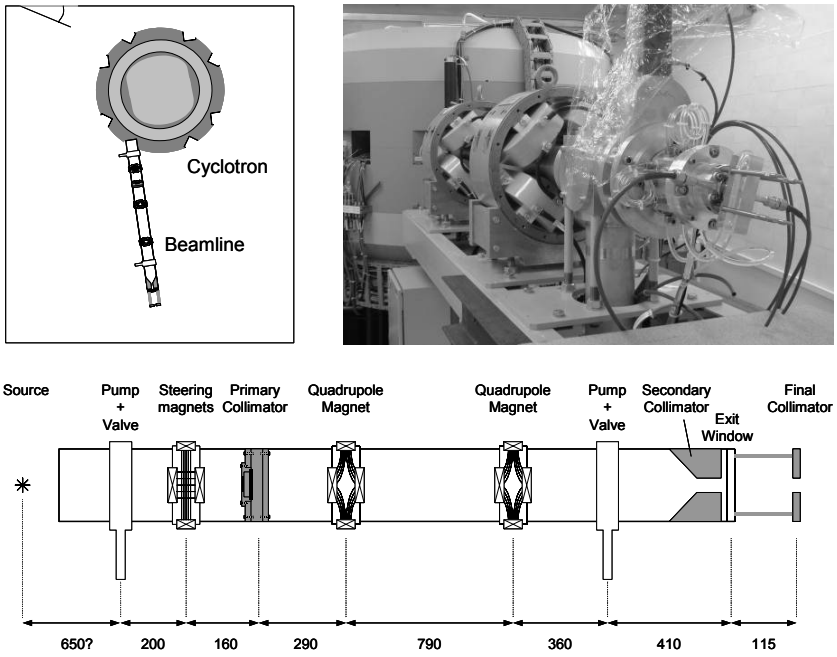

Figure 2. Schematic drawings and photograph of the beam line as used for the measurements in this report (drawings not to scale).

The two quadrupole magnets provide two free variables for adjusting the beam. That is why only two beam parameters can be controlled by the doublet. An extended flexibility could be achieved by moving the quadrupoles along the beam-line, which effectively means adding another free variable – the length of the drift space. This possibility was however practically limited by mechanical restrictions of the beam-line, which did not allow the positioning of the quadrupoles to an arbitrary position (because of the presence of vacuum valves and flanges limiting the space where the quadrupoles could be positioned). Moreover, while moving the quadrupoles could help to improve some beam-transport properties of the beam-line (for example to reduce the quadrupole strength), it could not change the basic qualitative feature of quadrupole focusing that is characterised by strong asymmetry between the horizontal and vertical plane. A quadrupole is a strong-focusing element with focusing action in one plane and defocusing action in the other plane. That is why focusing in both planes simultaneously can only be achieved by a proper combination of two quadrupoles forming a doublet. Two beam parameters can be controlled by varying the setting of the quadrupole doublet. If the beam-size in the horizontal plane and the beam-size in the vertical plane are controlled, then it is not possible to adjust at the same time the beam-divergence.

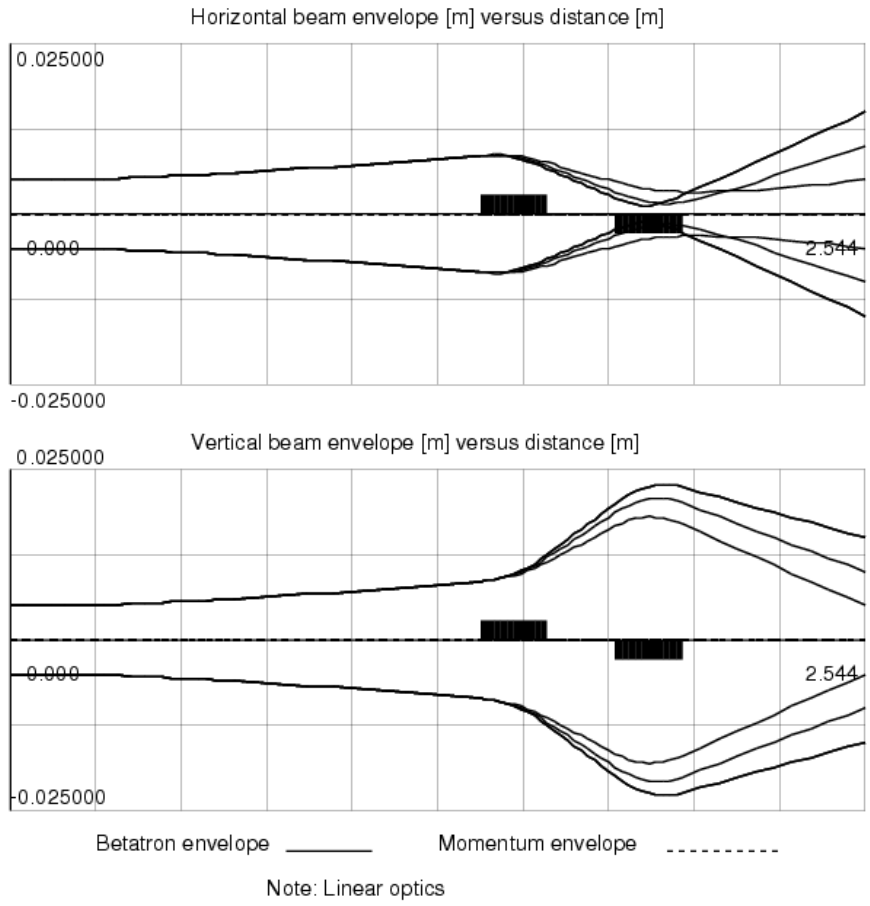

Figure 3. Beam-envelopes along the extraction channel for different settings of the quadrupole doublet. Exit beta-functions of 1 m, 4 m and 9 m correspond to the beam-size (RMS) of 5 mm, 10 mm and 15 mm, respectively. Upper plot – horizontal plane, lower plot – vertical plane.

Figure 3 demonstrates the focusing / defocusing action of the quadrupole doublet. We assumed the incoming beam parameters at the beginning of the beam line:

Beta-functions (horizontal / vertical): $\beta_x = \beta_z = 1$ m

Horizontal and vertical waist: $\alpha_x = \alpha_z = 0$

Beam-emittance (RMS, geometrical): $\varepsilon_x = \varepsilon_z = 25\pi$ mm·mrad

This leads to the input beam-size (RMS) of $\sqrt{\beta\varepsilon}$ = 5 mm in both planes. Different settings of the quadrupole doublet have been found to vary the beta-function at the exit of the beam-line. The beta-function of 1 m, 4 m and 9 m corresponds to the output beam-size (RMS) of 5 mm, 10 mm and 15 mm, respectively. The beam-envelopes corresponding to these three settings are shown in figure 3. The beam-transport simulations have been performed by WinAGILE computer code and checked independently by TRANSPORT.

It can be seen, that in all cases, the beam-divergence of the output beam is strongly asymmetric. The beam is diverging in the horizontal plane and converging in the vertical plane. For this reason, using the quadrupole doublet for spreading the beam is not recommended and the system with two collimators has been preferred.

2.1.2. Primary collimator

Details and photographs of the primary collimator are shown in figure 4. A system of three aluminium rings (Dural) blocks of the outer radii of the beam pipe for the proton beam whilst ensuring continuity of the vacuum. The first ring accommodates the actual pure aluminium collimator (99.99% Al), which in this case was like a sieve of 32 pinholes with a diameter of 0.25 mm and a length of 4 mm. Downstream the collimator a 50 μm thick pure aluminium scatter foil (99.99% Al) was attached. Vent holes were made in the foil for settling of the vacuum between the collimator and the scatter foil.

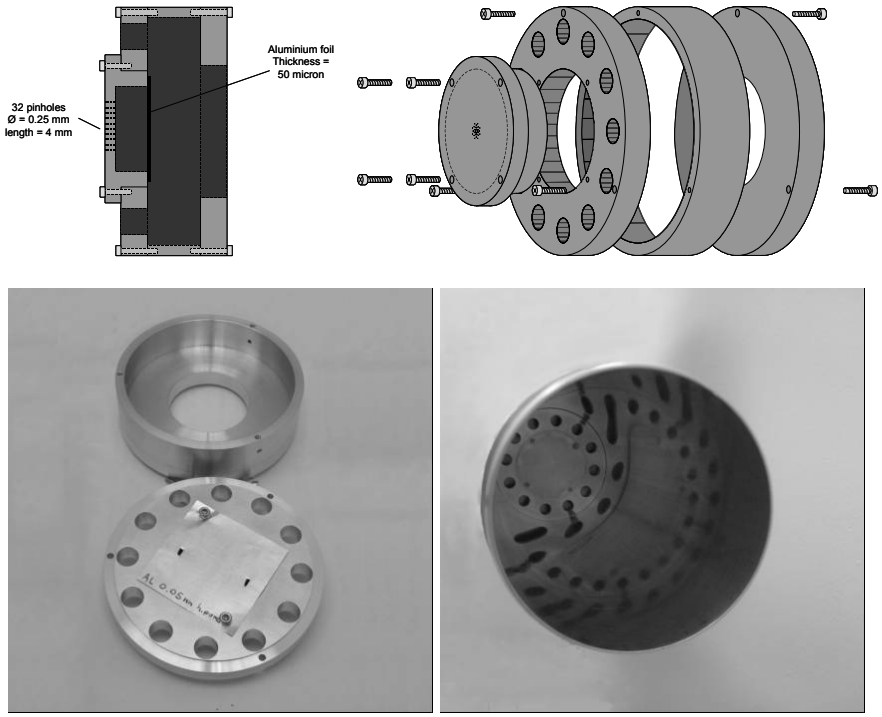

Figure 4. Upper left: detail of the collimator, including the aluminium scatter foil downstream of the pinhole collimator (not to scale). Upper right: assembly of collimator. Lower left: photograph of the scatter foil mounted to the back of the primary collimator. Lower right: photograph of the collimator mounted in the beam pipe.

2.1.3. Dosimetry set-up

The phantom was positioned on a small table moveable by a screw in the vertical direction. In the direction of the beam and in the horizontal lateral direction reproducible positioning of the phantoms was achieved by attaching spacer blocks to the table. If the transmission

ionization chamber was used, it was clamped between two spacer blocks as illustrated in figure 5. This set-up could be improved, especially regarding the alignment of the chambers and phantoms with the beam line.

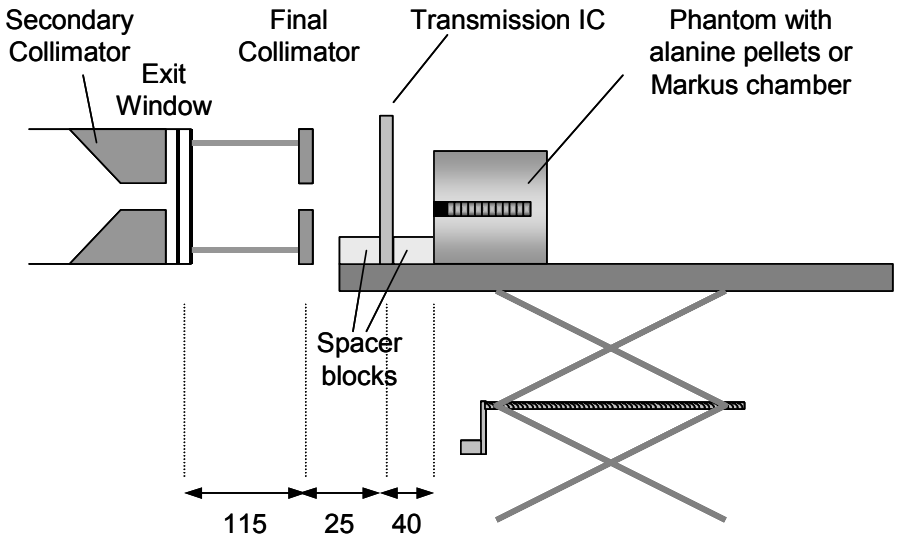

Figure 5. Set-up of the transmission ionization chamber and the phantom (not to scale).

2.2. Monte Carlo simulations

Monte Carlo simulations were performed for design purposes and for interpretation of the experimental data using the codes SRIM, MCNPX, McPTRAN.MEDIA and McPTRAN.RZ. They are described below before a description of the simulation geometries is given. Each of those codes has different abilities, which makes each of them suitable for particular applications. The first aim was to compare the three codes in some reference simulations to ensure that they are compatible. Then a number of simulations are performed supporting the experiments of this work.

2.2.1. SRIM (Stopping Power and Range of Ions in Matter)

SRIM-2003 (Ziegler and Biersack, 2003) is a software package for calculating the stopping and range of ions into matter mainly built around the older Monte Carlo code TRIM (the Transport of Ions in Matter). TRIM simulates transport of ions through a target made of compound materials with up to eight layers, each of which can consist of a different material. It scores the final 3D distribution of the ions as well as the distributions of energy loss, target damage, sputtering, ionization and phonon production. The energy range covered is 10 eV to 2 GeV per atomic mass unit. No secondary particles are tracked. The Monte Carlo code uses a condensed history algorithm with screened Coulomb collisions, including exchange and correlation interactions between the overlapping electron shells. The ions have long-range interactions creating electron excitations and plasmons within the target. The charge state of the ion within the target is described using the concept of effective charge, which includes a velocity dependent charge state and long range screening due to the collective electron sea of the target.

2.2.2. MCNPX (Monte Carlo N-Particle Transport Code System for Multiparticle and High Energy Applications)

MCNPX (Waters, 2002) is a general purpose Monte Carlo radiation transport code that tracks all element particles up to GeV range energies. Version MCNPX 2.4.0 combines MCNP4C3, a general purpose, continuous energy, generalised geometry, time dependent, coupled neutron-photon-electron Monte Carlo transport codesystem for energies up to 20 MeV and MCNPX 2.3.0 the previous version of MCNPX, LAHET 2.8 a code system for high energy particle transport calculations (in particular nucleons and pions in the medium energy range) and CEM a cascade exciton model for nuclear reactions by the Monte-Carlo method. It is a very versatile code system of which the most important feature for this work are a condensed history scheme for electromagnetic proton interactions, non-elastic nuclear interactions and transport of secondary particle cascades from nuclear interactions. Arbitrary three-dimensional configuration of materials in geometric cells bounded by first- and second-degree surfaces and some special fourth-degree surfaces can be treated. For the lower energy region of neutrons and photons pointwise continuous-energy cross section data are used. It contains intermediate interaction physics includes models for - Intranuclear Cascade Models - Multistage Pre-equilibrium Models (MPM) - Fermi-Breakup Model - Evaporation Model - Level Densities - High-Energy Fission - High-Energy Interactions contains an early version of the FLUKA high-energy code. A variety of variance reduction techniques, scoring tallies and data analysis tools are included. The simulated particle range (relevant for this work) is restricted to neutrons in the LA150 library from 0.0 - 150.0 MeV in tabular range for 42 isotopes (except for 9Be to 100 MeV), neutrons from 1.0 MeV in physics model regime, protons from 1.0 to 150.0 MeV in tabular range for 41 isotopes, protons from 1.0 MeV in physics model regime, photons from 1 keV - 100 GeV and photonuclear interactions from 1.0 to 150.0 MeV in tabular range for 12 isotopes.

2.2.3. McPTRAN.MEDIA and McPTRAN.RZ

This codes are derived from PTRAN (Berger, 1993), which uses the Monte Carlo method to simulate the transport of proton beams in water for protons with energies under 255 MeV. Multiple scattering and Coulomb interaction energy loss mechanisms are taken into account along with nonelastic nuclear interactions. PTRAN calculates deposition of energy as a function of depth and radial distance from the beam, energy spectra of the primary protons as function of depth. The code uses a condensed-random-walk Monte Carlo scheme (Berger, 1963), and takes into account energy-loss straggling in Coulomb collisions with atomic electrons, multiple-scattering deflections due to elastic scattering by atoms and energy loss in nonelastic nuclear reactions. Secondary particles are not tracked.

Due to the limited geometrical range that can be simulated, codes that enable simulation in other materials than water and for more complex geometries were developed. These programs are described by Palmans (2005) and comprise McPTRAN.MEDIA, for simulating transport through a succession of slabs that can each have a different material composition, and McPTRAN.RZ, which in addition include the definition of a number of concentric cylinders perpendicularly to the slabs allowing a different material between any two of the cylindrical surfaces within one slab as shown in figure 6. McPTRAN.RZ enables the calculation of energy deposition of dose in each rz-voxel as well as the calculation of spectral particle fluence distributions differential in energy and angle.

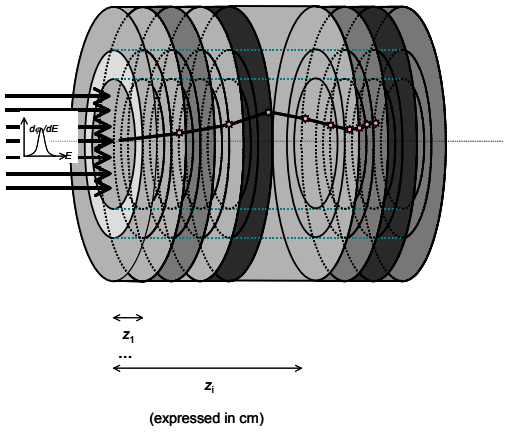

Figure 6. Geometry for McPTRAN.RZ.

The implementation of these extensions to PTRAN required modifications to the material data generation programs, the scoring algorithms and the transport algorithm, especially with respect to the crossing of boundaries. These are described in detail by Palmans (2005). For this work a slight modification was required to McPTRAN.RZ in order to enable the simulation of particle drift in vacuum as a possible medium in the voxel geometry.

2.2.4. Simulated geometries

With one or more of the codes discussed above, the following problems were calculated:

(i) Energy loss and spectral widening of 18 MeV protons through slabs of water, alanine, air, graphite, aluminium, titanium and copper. The aim of these simulations was to learn on the one hand how much material could be acceptably placed in the beam path for various purposes (vacuum window, distance air gap, scattering foil, transmission monitor, etc.) and on the other hand whether or not there would be any advantage in using one or another material as scatterer. An additional goal was to identify in a simple geometry the differences between the three Monte Carlo codes and the range of applications for which each of them would be suitable. These simulations were performed with SRIM, MCNPX and McPTRAN.MEDIA.

(ii) Neutron and gamma production on graphite, aluminium and copper as target materials was calculated using MCNPX to characterise them as collimator materials.

(iii) Geometry of an initially proposed experimental set-up with a stack of alanine pellets located in a PMMA phantom. The geometry of these simulations is shown in figure 7. These simulations were performed with MCNPX and McPTRAN.RZ for either a proton point source located 2 m from the exit window or a pencil beam with a diameter of 1 mm.

(iv) Geometry of the experimental set-up used during the measurement with a stack of alanine pellets located in a PMMA phantom. The geometry of these simulations is shown in figure 8. These simulations were performed McPTRAN.RZ for either a proton point source or a pencil beam with a diameter of 1 mm. The distances were taken according to figure 2. For the primary collimator hole diameters of 0.25 mm, 1 mm and 2 mm were simulated. The primary scatter foil was 50 µm aluminium and the dual exit window consisted of two 25 µm aluminium foils. The secondary collimator was given a hole diameter of 12 mm but the preceding conical part was not simulated. The source was given an offset from the beam

axis such that the incident angle varied between 0 and 3 degrees. This angle is called the source angle in the remainder of this report. Apart from the introduction of this source angle, the main difference between these and earlier simulations is that all the distances between collimators, scatter foil, exit window and phantom are close (within about 1 cm) to the conditions of the experimental run.

(a)

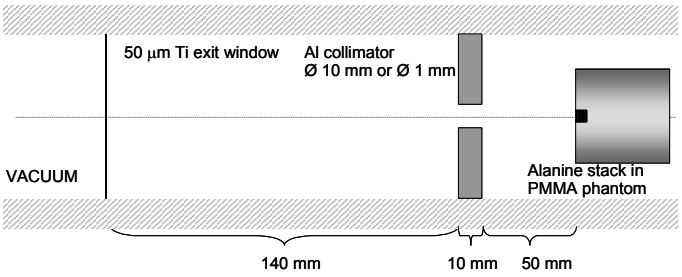

(b)

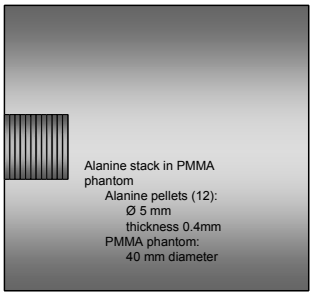

Figure 7. Schematic drawing of the simulated geometry of a stack of alanine pellets in a PMMA phantom according to a first proposal for the beam line (a) including the end of the vacuum pipe and titanium exit window and (b) detail of the phantom.

Since the latter calculations were very inefficient (especially those with source angles of 2 and 3 degrees) some additional modifications were introduced in McPTRAN.RZ. A new source type was introduced to emit particles only in a solid angle specified by limiting values of azimuthal and polar angles (in the previous version particles were only limited between azimuthal angles of zero and a specified maximum value). This new feature was used to specify for each simulation a solid angle that covered a bit more than the area of the primary collimator hole. The calculated results were then normalized to a common solid angle corresponding to a projected area on the primary collimator entrance plane of 1 cm^2. Another modification that was made to the code was the introduction of range rejection (i.e. if the distance of the proton to the nearest plane in a region is larger than its maximum range, its energy is deposited locally). This results in an error since no nuclear attenuation is taken into account for the remainder of the path the particle would travel. Therefore it was only applied in the collimator regions where we are not interested in the dose deposition.

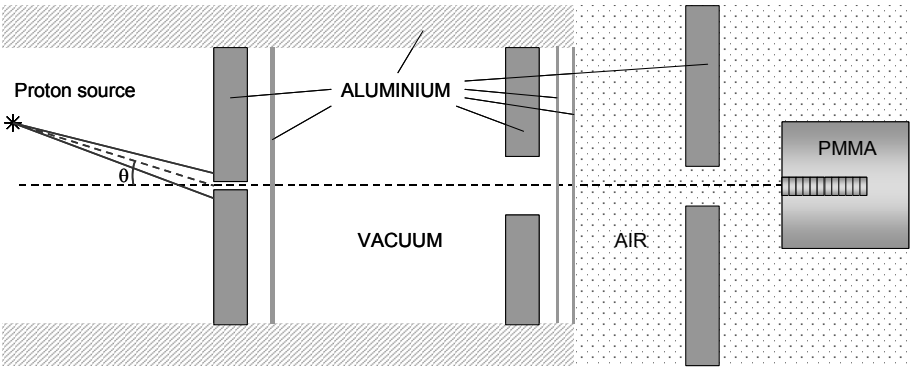

Figure 8. Schematic drawing of the simulated geometry of the beam line and a stack of alanine pellets in a PMMA phantom according to the conditions during the experiments (not to scale).

2.3. Radiochromic film measurements

Two types of radiochromic films were available: GafChromic EBT film, which has a blue appearance and gets more opaque after exposure, and RTQA film, which has an orange appearance and gets brown to black after exposure. After exposure, the films were digitised with a digital camera and converted to 8 bit gray scale. These two film types have a relatively high sensitivity and the maximum dose up to which their response is linear is about 8 Gy.

Lateral profiles were measured twice at the surface of the phantom and once immediately outside the exit window. Figure 9 illustrates how a depth dose distribution was measured by squeezing a piece of EBT GafChromic film between two slabs of PMMA and tilting the phantom slightly with respect to the beam axis.

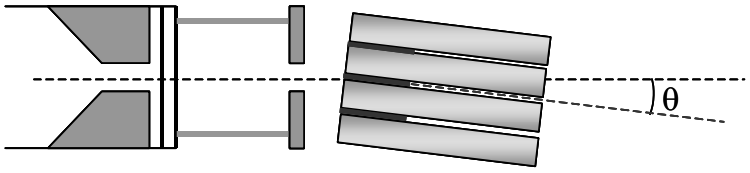

Figure 9. Set-up for a depth dose measurement using GafChromic EBT film squeezed between PMMA slabs.

2.4. Alanine experiments

Two alanine experiments were performed; one to determine the relative RE as a function of depth and one to determine the absolute RE by direct comparison with an ionization chamber. Both set-ups are shown in figure 10.

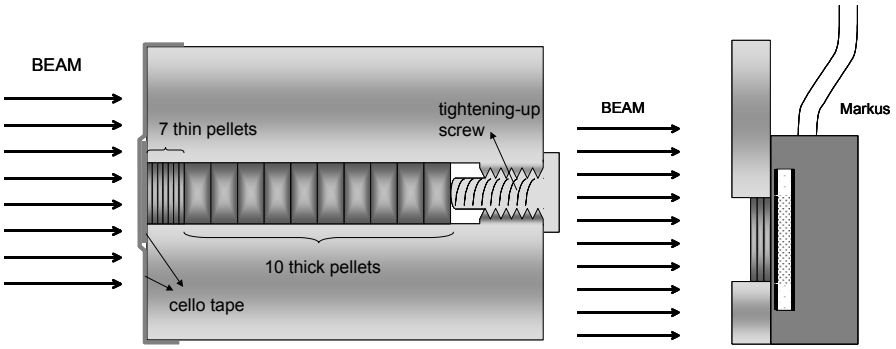

Figure 10. Two set-ups used for alanine irradiations. Left: a stack of pellets in PMMA for measuring relative RE as a function of depth. Right: three pellets in PMMA for direct comparison with a Markus ionization chamber.

For the relative measurements seven thin pellets (nominal thickness 0.5 mm) are aligned with the surface of a small PMMA phantom using a double layer of cello tape. Ten thick pellets (nominal thickness 2.5 mm) are used as backing to fill up the phantom and a screw tightens up the stack.

For the absolute measurements a 5.1 mm diameter hole was drilled in a 3.5 mm thick slab of PMMA. Three pellets were then held at the back of this hole touching the front window of the Markus chamber. The advantage of this set-up is that there is a high degree of correlation between the proton fluence seen by the alanine pellets and the proton fluence seen by the Markus ionization chamber since the sensitive area perpendicular to the beam axis is almost the same for both detectors (5 mm diameter for the pellets and 5.3 mm for the Markus chamber). On the other hand, the edges of PMMA, which are considerably thicker than the three pellets combined, might cause a perturbation difficult to calculate.

The Markus chamber has a calibration factor $N_{D,w,\mathrm{Co\text{-}60}}$ in terms of absorbed dose to water in ^{60}Co. Absorbed dose to water $D_{w,p}$ in the proton beam quality p was obtained from the charge M_p collected by the Markus chamber (corrected for temperature and pressure) by applying IAEA TRS-398 (Andreo et al. 2000), i.e.

$$D_{w,p} = M_p \, N_{D,w,\mathrm{Co\text{-}60}} \, k_{p,\mathrm{Co\text{-}60}}$$

where $k_{p,\mathrm{Co\text{-}60}}$ is the beam quality correction factor that converts the absorbed dose to water calibration factor from the calibration beam quality to the proton beam quality. IAEA TRS-398 tabulates $k_{p,\mathrm{Co\text{-}60}}$ only down to a residual range of 0.25 cm. Assuming the beam quality in our case to correspond to 0.15 cm, a linear extrapolation in a log-log scale results in $k_{p,\mathrm{Co\text{-}60}} = 1.011$, whereas a quadratic extrapolation results in $k_{p,\mathrm{Co\text{-}60}} = 1.014$. The average value of $k_{p,\mathrm{Co\text{-}60}} = 1.013$ was taken for the present work.

Finally, dose to water obtained with the Markus chamber was multiplied with a factor of $(0.53/0.50)^2$ to account for the fraction of the sensitive volume of the ionization chamber that is shielded from the beam.

3. RESULTS

3.1. Monte Carlo calculations

3.1.1. Energy degradation and scatter by various absorbers

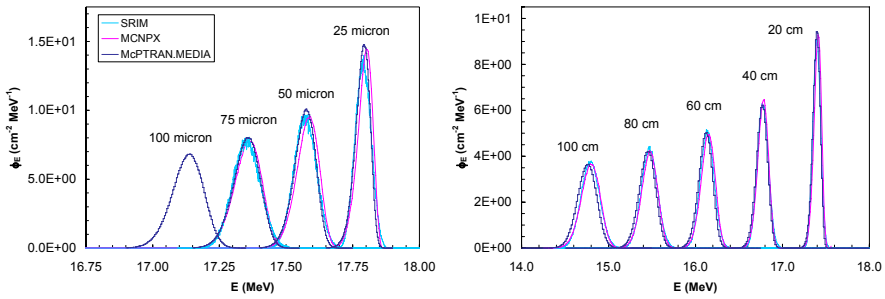

Figure 11. Energy spectra of protons traversing a layer of titanium (left) or air (right) with varying thickness obtained with SRIM, MCNPX and McPTRAN.MEDIA.

In the first proposal for the beam line, the exit window was foreseen to be titanium with a preferred minimum thickness of 50 μm. The energy spread of 18 MeV protons after traversing various thin titanium layers are shown in figure 11, calculated with the three Monte Carlo codes. This represents various possible thicknesses of the titanium vacuum exit window. Table 2 gives the energy at the maximum, the mean energy and the full width at half maximum (FWHM). Both the figure and the table show that there is a good agreement between the three codes.

Table 2. Some parameters characterising the spectra of figure 11 for titanium.

Ti window (μm) →	25	50	75	100
E_{max} (SRIM)	17.79	17.58	17.36	
E_{max} (MCNPX)	17.80	17.59	17.36	
E_{max} (PTRAN)	17.79	17.58	17.36	17.15
E_{mean} (SRIM)	17.79	17.57	17.35	
E_{mean} (MCNPX)	17.79	17.58	17.35	
E_{mean} (PTRAN)	17.79	17.57	17.35	17.13
FWHM (SRIM)	0.070	0.097	0.117	
FWHM (MCNPX)	0.064	0.100	0.120	
FWHM (PTRAN)	0.060	0.090	0.110	0.140

After the exit window there is an air gap before the proton beam enters the phantom. With the low-energy protons of this experiment, the energy loss over this air gap can be significant. The energy spectra of 18 MeV mono-energetic protons after traversing air columns of varying thickness are also shown in figure 11, calculated with the three Monte Carlo codes. The thickness of the air column represents the distance from the exit window

where the experiment takes place. Table 3 gives the energy at the maximum, the mean energy and the full width at half maximum (FWHM). Both the figure and the table show that there is a good agreement between the three codes.

The average energy loss over the air gap is significant and the air gap should thus be kept to a minimum. However, some space is needed for sufficient spreading out of the beam by the second scatter foil. 20 cm could be considered reasonable although it is short for the effect of the scatter foil. Figure 12 illustrates how the beam size changes with varying thickness of the air column and how the combined beam widening effect due to the scatter of the exit window and the air column results in considerable beam flattening.

Table 3. Some parameters characterising the spectra of figure 11 for air.

Depth (cm)	20	40	60	80	100
E_{max} (SRIM)	17.40	16.77	16.13	15.48	14.80
E_{max} (MCNPX)	17.41	16.79	16.16	15.47	14.80
E_{max} (McPTRAN)	17.40	16.77	16.13	15.45	14.77
E_{mean} (SRIM)	17.40	16.77	16.13	15.47	14.79
E_{mean} (MCNPX)	17.40	16.77	16.14	15.46	14.78
E_{mean} (McPTRAN)	17.39	16.76	16.11	15.44	14.75
FWHM (SRIM)	0.105	0.150	0.175	0.215	0.250
FWHM (MCNPX)	0.100	0.150	0.190	0.210	0.250
FWHM (McPTRAN)	0.100	0.150	0.180	0.225	0.255

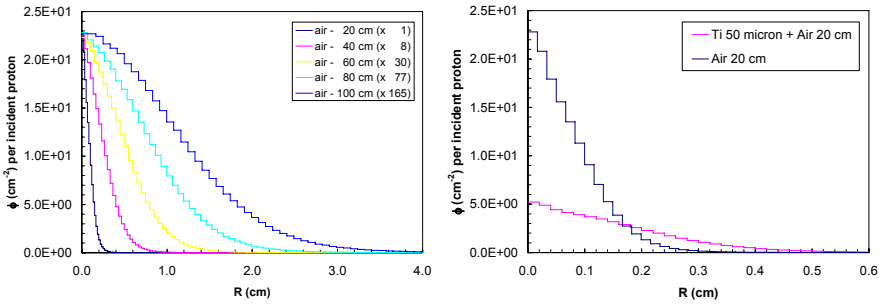

Figure 12. Left: Radial distribution of proton fluence after traversing a layer of air with varying thickness obtained with McPTRAN.MEDIA. All distributions are normalized at r = 0 to coincide with the 20 cm curve. Right: Radial distribution of proton fluence after traversing a 20 cm layer of air either combined with or without the effect of a 50 µm titanium window.

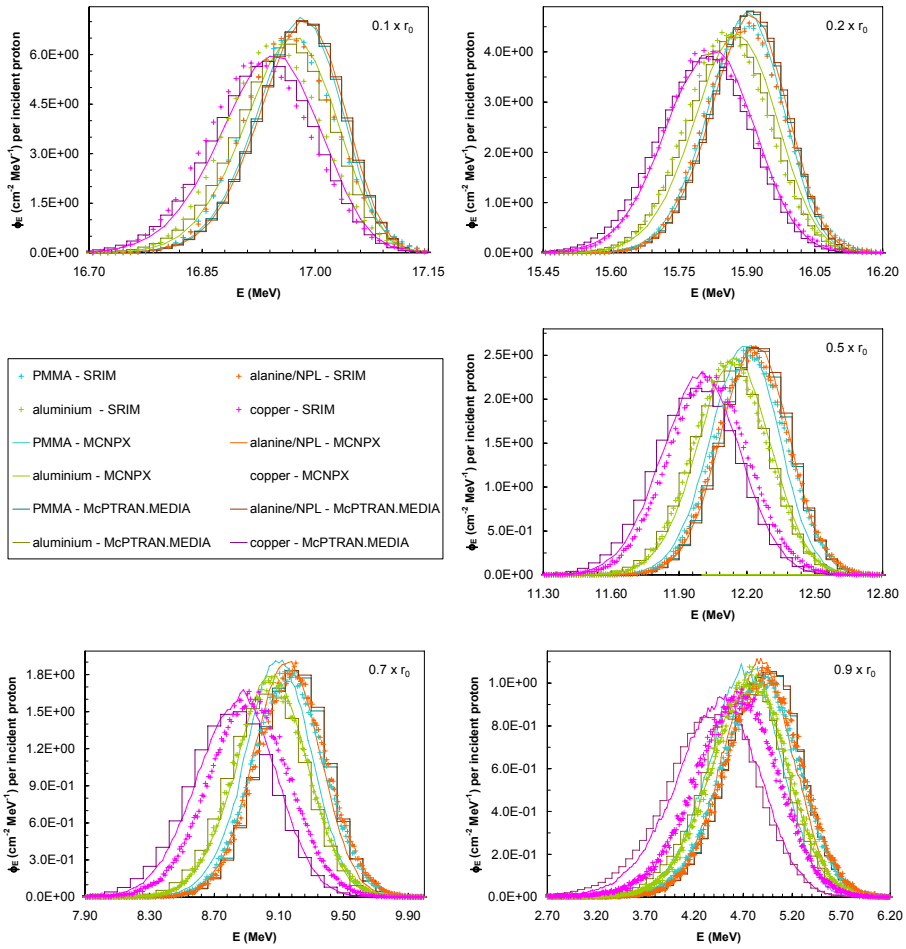

Figure 13. Energy spectra of protons traversing layers of PMMA, alanine (NPL pellet composition), aluminium and copper with varying thickness obtained with SRIM, MCNPX and McPTRAN.MEDIA.

Energy spectra for 18 MeV mono-energetic protons after traversing layers of several materials that will be used in the measurements with varying thickness are shown in figure 13, calculated with the three Monte Carlo codes. Table 4 gives the energy at the maximum, the mean energy and the full width at half maximum (FWHM) for all situations. Both the figure and the table show that there is a good agreement between the three codes. They also show that simple range scaling is sufficiently accurate to obtain the proton spectrum after traversing low-Z materials. This is important since different low-Z materials will be present in the beam path from the source to the detector.

Radial distributions of proton fluence for 18 MeV mono-energetic protons after traversing layers of several materials that will be used in the measurements with varying thickness are shown in figure 14, calculated with MCNPX and McPTRAN.MEDIA. All are calculated at 90% of the csda range. These graphs show that there is are some differences in the radial distributions, which can be related to the different multiple scattering models used in both codes. The differences are not relevant for beam widening effects such as in the penumbra of a broad beam when penetrating a solid phantom. Although the effects will be less when thinner slabs are considered, they might be substantial enough to be of concern when the effect of scatter windows will be investigated. This will be discussed below.

Table 4. Some parameters characterising the spectra of figure 13.

Depth (z/r0)	0.1	0.2	0.3	0.4	0.5	0.6	0.7	0.8	0.9	1
PMMA										
E_{max} (SRIM)	16.97	15.89	14.76	13.56	12.21	10.76	9.17	7.32	4.85	0.94
E_{max} (MCNPX)	16.97	15.89			12.21		9.11		4.67	
E_{max} (PTRAN)	16.98	15.91	14.76	13.56	12.23	10.84	9.18	7.33	5.01	1.18
E_{mean} (SRIM)	16.96	15.90	14.76	13.53	12.21	10.77	9.15	7.27	4.86	1.08
E_{mean} (MCNPX)	16.96	15.88			12.17		9.07		4.68	
E_{mean} (PTRAN)	16.98	15.90	14.76	13.54	12.23	10.79	9.18	7.30	4.90	1.19
FWHM (SRIM)	0.150	0.210	0.260	0.310	0.370	0.420	0.510	0.630	0.880	1.790
FWHM (MCNPX)	0.140	0.180			0.360		0.480		0.840	
FWHM (PTRAN)	0.135	0.195	0.250	0.300	0.350	0.480	0.560	0.630	0.840	
air										
E_{max} (PTRAN)	16.98	15.91	14.76	13.53	12.23	10.76	9.18	7.33	4.87	1.06
E_{mean} (PTRAN)	16.97	15.89	14.75	13.53	12.21	10.77	9.15	7.26	4.85	1.17
FWHM (PTRAN)	0.135	0.195	0.250	0.300	0.350	0.400	0.480	0.630	0.910	
alanine pellet NPL										
E_{max} (SRIM)	16.97	15.91	14.78	13.55	12.22	10.80	9.21	7.33	9.86	2.41
E_{max} (MCNPX)	16.97	15.89			12.23		9.17		4.87	
E_{max} (PTRAN)	16.98	15.91	14.76	13.56	12.23	10.84	9.18	7.33	5.01	1.10
E_{mean} (SRIM)	16.96	15.89	14.75	13.54	12.23	10.79	9.18	7.28	4.89	1.28
E_{mean} (MCNPX)	16.97	15.89			12.22		9.13		4.81	
E_{mean} (PTRAN)	16.98	15.90	14.76	13.55	12.24	10.80	9.18	7.30	4.90	1.19
FWHM (SRIM)	0.150	0.210	0.270	0.310	0.370	0.430	0.500	0.600	0.890	1.680
FWHM (MCNPX)	0.140	0.200			0.360		0.480		0.840	
FWHM (PTRAN)	0.135	0.195	0.250	0.300	0.350	0.480	0.560	0.630	0.840	
aluminium										
E_{max} (SRIM)	16.95	15.85	14.69	13.48	12.16	10.68	9.08	7.21	4.77	1.03
E_{max} (MCNPX)	16.97	15.87			12.13		9.07		4.83	
E_{max} (PTRAN)	16.97	15.86	14.69	13.47	12.13	10.68	9.02	7.15	4.80	0.58
E_{mean} (SRIM)	16.95	15.85	14.69	13.46	12.12	10.67	9.05	7.15	4.75	1.09
E_{mean} (MCNPX)	16.95	15.86			12.13		9.04		4.72	
E_{mean} (PTRAN)	16.96	15.86	14.70	13.46	12.12	10.66	9.02	7.11	4.69	1.07
FWHM (SRIM)	0.150	0.210	0.270	0.330	0.390	0.440	0.530	0.640	0.890	1.810
FWHM (MCNPX)	0.140	0.220			0.380		0.500		0.880	
FWHM (PTRAN)	0.150	0.225	0.300	0.330	0.450	0.480	0.560	0.720	0.980	
titanium										
E_{max} (PTRAN)	16.95	15.85	14.66	13.44	12.08	10.60	8.94	7.06	4.66	0.62
E_{mean} (PTRAN)	16.94	15.84	14.66	13.41	12.07	10.59	8.94	7.01	4.55	1.04
FWHM (PTRAN)	0.150	0.240	0.300	0.360	0.450	0.560	0.560	0.720	1.050	
copper										
E_{max} (SRIM)	16.92	15.81	14.65	13.40	12.01	10.54	8.92	6.97	4.69	1.08
E_{max} (MCNPX)	16.93	15.83			11.99		8.87		4.51	
E_{max} (PTRAN)	16.94	15.82	14.61	13.35	11.98	10.52	8.86	6.88	4.45	0.66
E_{mean} (SRIM)	16.93	15.82	14.64	13.37	12.03	10.54	8.91	6.98	4.60	1.11
E_{mean} (MCNPX)	16.93	15.80			11.98		8.82		4.40	
E_{mean} (PTRAN)	16.93	15.80	14.61	13.34	11.97	10.47	8.80	6.84	4.34	1.15
FWHM (SRIM)	0.170	0.230	0.300	0.350	0.400	0.500	0.560	0.700	0.950	1.790
FWHM (MCNPX)	0.160	0.220			0.400		0.560		0.980	
FWHM (PTRAN)	0.165	0.240	0.325	0.390	0.450	0.480	0.640	0.720	1.050	

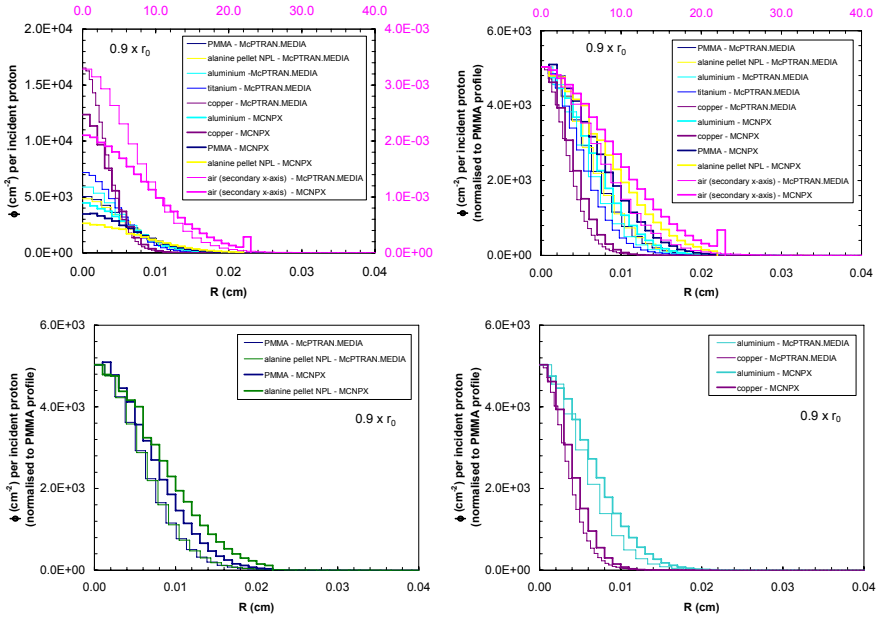

Figure 14. Radial distributions of proton fluence after traversing layers of PMMA, alanine (NPL pellet composition), aluminium and copper with a thickness equalling 90% of the csda range obtained with MCNPX and McPTRAN.MEDIA. Various normalisation were done for visualisation purposes.

3.1.2. Depth dose distributions

Figure 15 shows depth dose distributions for PMMA and alanine (NPL mixture of 90% alanine and 10% paraffin) calculated using the three Monte Carlo codes. The calculations were for a pencil beam incident on a cylindrical tube of 5 mm diameter. The lateral scatter of the beam is such that no primary protons escape the tube. The agreement is in general good, with the exception of the simulation for alanine pellets with MCNPX. The small differences for the other materials, as well as the anomalous MCNPX result can be explained by the mass stopping powers used.

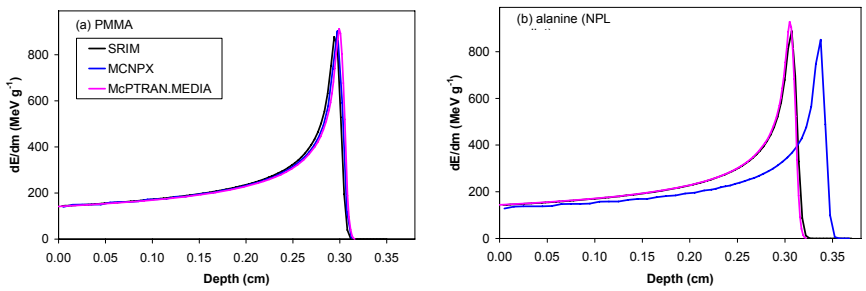

Figure 15. Depth dose distributions in PMMA and alanine (NPL mixture of 90% alanine and 10% paraffin) obtained with SRIM, MCNPX and McPTRAN.MEDIA.

Stopping powers for alanine (NPL mixture of 90% alanine and 10% paraffin) in McPTRAN.MEDIA are calculated according to ICRU37 & ICRU49 including corrections for mean excitation energy (accounting for chemical state), density and Barkas correction (Palmans 2006). In SRIM they calculated including correction factor accounting with

structure formula of molecules (both alanine and paraffin). In MCNPX, on the other hand, stopping powers are calculated from elemental composition without any further sophistication regarding chemical composition. Figure 16 shows that this results in stopping power values that are substantially different. The about 10% lower stopping power values in MCNPX explain the about 10% larger range.

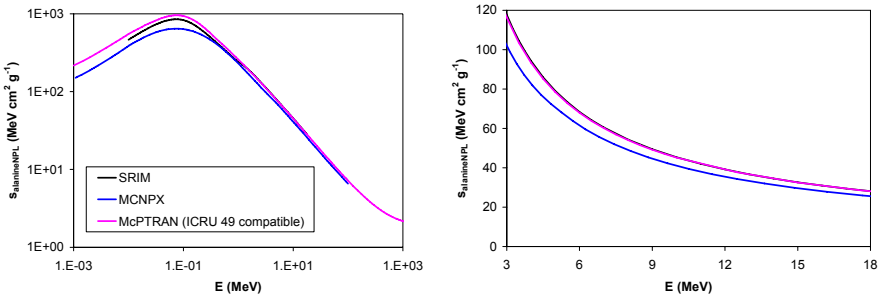

Figure 16. Comparison between stopping powers used in SRIM, MCNPX and McPTRAN.MEDIA.

Since in the energy range above a few MeV the difference in stopping powers between McPTRAN.MEDIA and MCNPX could be characterised by a single multiplicative factor, the density of alanine pellets was artificially increased from 1.15 g cm^{-3} to 1.27 g cm^{-3} in subsequent calculations in order to account for this difference.

3.1.3. Neutron and gamma contribution from collimator material

As mentioned before, one of the functions of the primary collimator was to reduce the beam current by more than two orders of magnitude. An estimate was made by a Monte Carlo simulation with MCNPX of how much the neutron and gamma fluence due to aluminium or copper primary collimators at the measurement set-up would be. Theoretical estimates using the nonelastic nuclear interaction data from ICRU report 63 were made as well assuming complete stopping of protons ignoring any attenuation effect (which is especially for gammas important in the comparison with the MCNPX data).

Table 5. Number of neutrons (n) and gamma photons (γ) produced per stopped proton in copper or aluminium and the resulting fluence at the alanine set-up per proton reaching this set-up (assuming 1% of all protons is stopped in primary collimator).

	# per p stopped		Φ (cm^{-2}) per p at 2m	
	n	γ	n	γ
Copper				
MCNPX 1 cm	0.0035	0.0096	7.0×10^{-7}	1.9×10^{-6}
MCNPX 5 cm	0.0035	0.0059	7.0×10^{-7}	1.2×10^{-6}
ICRU-63	0.0023	0.0127	4.7×10^{-7}	2.5×10^{-6}
Aluminium				
MCNPX 1 cm	0.0006	0.0130	1.2×10^{-7}	2.6×10^{-6}
ICRU-63	0.0008	0.0115	1.6×10^{-7}	2.3×10^{-6}

The results are presented in table 5 showing that per proton stopped in a 1 cm thick copper collimator, about 0.003 neutrons and 0.01 gamma photons are produced. This result in less than 10^{-8} neutrons and around 2×10^{-8} gamma photons per cm^2 at the alanine set-up. If 99% is stopped than this is 0.3 neutrons and 1 gamma photon per proton that arrives at the alanine set-up (assuming all transmitted protons arrive there) or less than 10^{-6} neutrons and around 10^{-6} gamma photons per cm^2 at alanine set-up. For a 1 cm diameter final collimator this could be increased by up to another two orders of magnitude depending on the emmitance after the primary collimator. Overall these neutron and gamma levels are considered to be insignificant, since dose deposition due to neutrons and gammas is orders of magnitude lower than of protons. At a collimator made of aluminium, the number of gamma photons produced is similar whereas the number of neutrons produced is almost an order of magnitude smaller than for a copper collimator. Theoretical estimates based on ICRU report 63 result in similar estimates as can be seen in table 5.

3.1.4. Stack of alanine pellets in PMMA phantom according to initial proposal

Figure 17 shows depth dose curves for the initially proposed beam line simulated with MCNPX and McPTRAN.RZ for mono-energetic protons and protons with a gaussian energy spread with a standard deviation of 1%. The dose per incident proton obtained with MCNPX was found to be slightly lower (about 20% for the 1 mm collimator and 10 % for the 10 mm collimator). It was observed that the number of protons that are transmitted through the final collimator is about the same amount lower in MCNPX than in McPTRAN. This can probably be related to the different multiple scatter model used in both codes. After normalization both codes agree well, indicating that the beam quality as modelled by both codes is in good agreement.

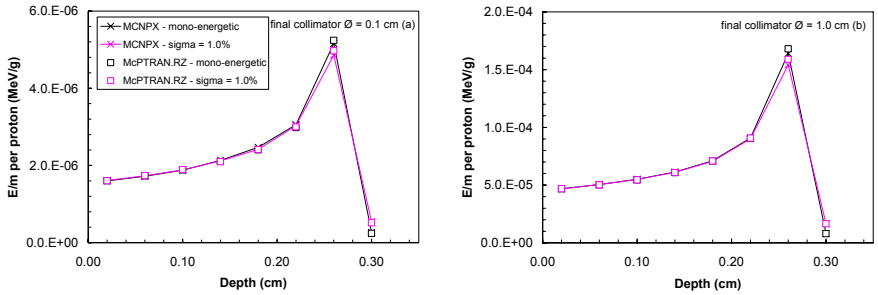

Figure 17. Dose in a stack of alanine pellets simulated according to the geometry of figure 7a using MCNPX and McPTRAN.RZ with a point source and for final collimator diameters of 1 mm (a) and 10 mm (b).

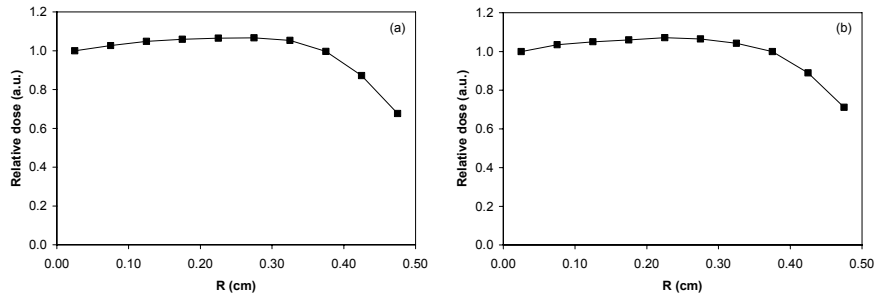

Figure 18. Lateral dose profiles at the phantom surface simulated according to the geometry of figure 7a using McPTRAN.RZ for a parallel beam with a diameter of 10 mm (a) and a point source (b).

Simulations of the lateral profiles with McPTRAN.RZ, shown in figure 18, show a reasonably good lateral homogeneity and, furthermore, that there is not much difference between the parallel beam and point source.

3.1.5. Depth dose in PMMA phantom according to real experimental set-up

As will be discussed in the experimental results, the experimental beam showed some unexpected behaviour in the sense that the characteristic Bragg peak was absent. In order to get a better understanding of this behaviour, additional Monte Carlo simulations were performed using McPTRAN.RZ and MCNPX, taking into account the approximate geometry used in the experiments.

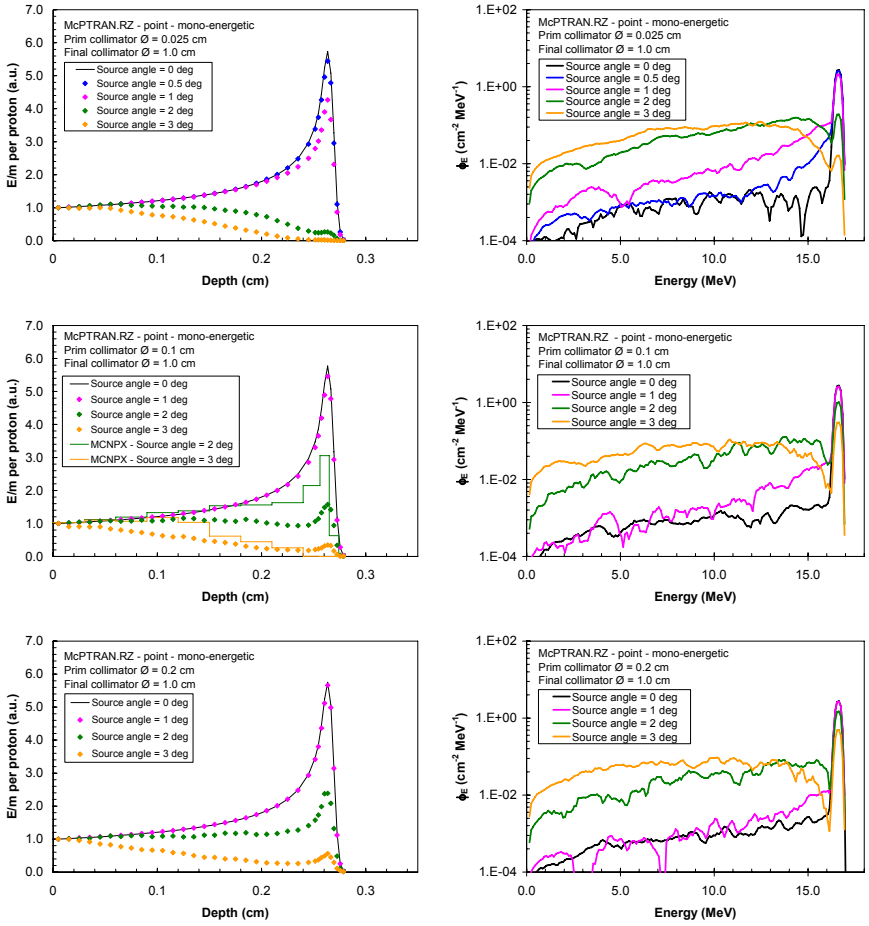

Figure 19. Left: depth dose profiles for three primary collimator sizes and for source angles ranging from 0 to 3 degrees simulated with McPTRAN.RZ. Two cases of the Ø 1 mm collimator with 2 and 3 degrees source angles simulated with MCNPX are shown as well. Right: corresponding proton spectra calculated at the surface of the phantom simulated with McPTRAN.RZ.

Figure 19 shows depth dose profiles in the PMMA phantom and proton spectra at the surface of the phantom for three primary collimator sizes and for source angles from 0 to 3 degrees. For the 1 mm primary collimator beam, the simulations with MCNPX for source angles of 0 and 1 degrees were consistent and only the results for source angle of 2 and 3 degrees are shown. The depth dose profiles were scored with a depth resolution of 1 mm

near the surface and with a finer grid near the Bragg peak. The size of the scoring voxels was 5 mm in diameter, corresponding to the size of the alanine pellets. All depth dose profiles were normalised to unity at the phantom surface. The proton spectra were scored in the 1 mm thick 5 mm diameter volume at the surface, so a slight broadening of the primary proton peak due to the finite volume of this scoring region is visible. All proton spectra are per incident photon on the phantom surface.

It can be seen that for the 0.25 mm diameter pinhole collimator, the Bragg peak visually reduces already from a 1 degree source angle and that it completely disappears for angles of 2 and 3 degrees. If we look at the corresponding proton spectra we see that the peak of primary protons reduces and that the low-energy tail grows with increasing source angle. The reductions seen in the MCNPX simulations are qualitatively similar but slightly different in magnitude than in the McPTRAN.RZ results, which can probably be explained by differences in the scattering and secondary particle production models used. These differences do not affect the quantitative conclusions below.

From a pure geometrical consideration it is clear that a proton incident under an angle of 3 degrees will not be able to transmit directly through the pinhole collimator, such that the only protons that get through have been scattered at the inner surface of this collimator and hence have lost part of their energy. For the collimator sizes of 1 and 2 mm the situation is better. At a source angle of 1 degree no visual effect occurs but at larger angles the contribution of low-energy protons increases again resulting in a collapse of the Bragg peak. This leads to the suggestion that using a larger collimator will improve the beam characteristics. It was also suggested that this would make the task of steering the beam straight through the collimator easier than with the pinhole-sieve collimator.

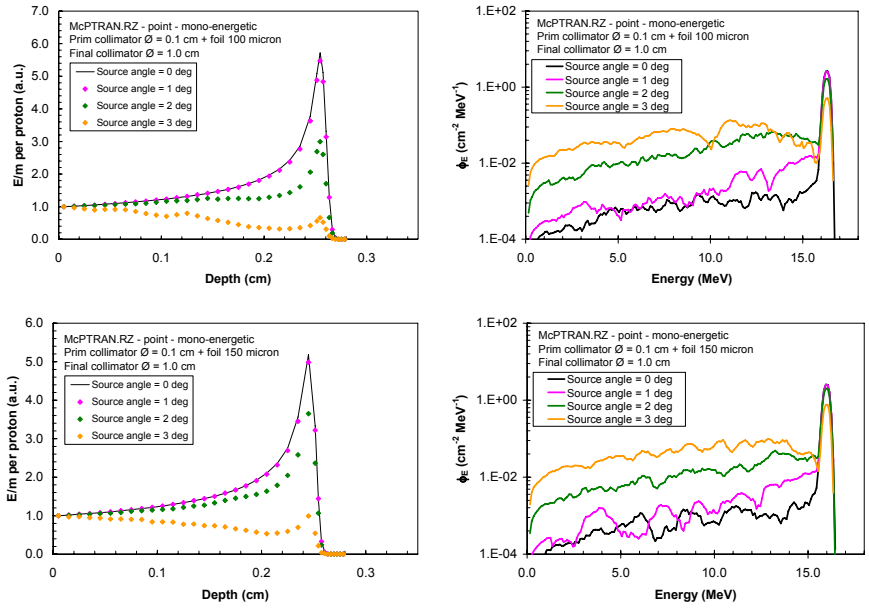

Figure 20. Left: depth dose profiles for a 100 µm primary scatter foil and a 150µm primary scatter foil combined with the 1 mm diameter primary collimator and for source angles ranging from 0 to 3 degrees. Right: corresponding proton spectra calculated at the surface of the phantom.

Further simulations were preformed using the 1 mm primary collimator in order to find other suggestions for improving the beam: simulations with a primary scatter foil of 100 µm

or 150 µm instead of 50 µm and simulations with absence of either the secondary collimator, the third collimator or both the second and third collimators. The depth dose distributions as a function of angle for the two thicker scatter foils are shown in figure 20 and clearly show an improvement of the depth dose and spectral characteristics. Of course this goes to the expense of the primary energy at the phantom surface and consequently of the range, but to the extent that this compromise is acceptable part of the solution could be to increase the foil thickness.

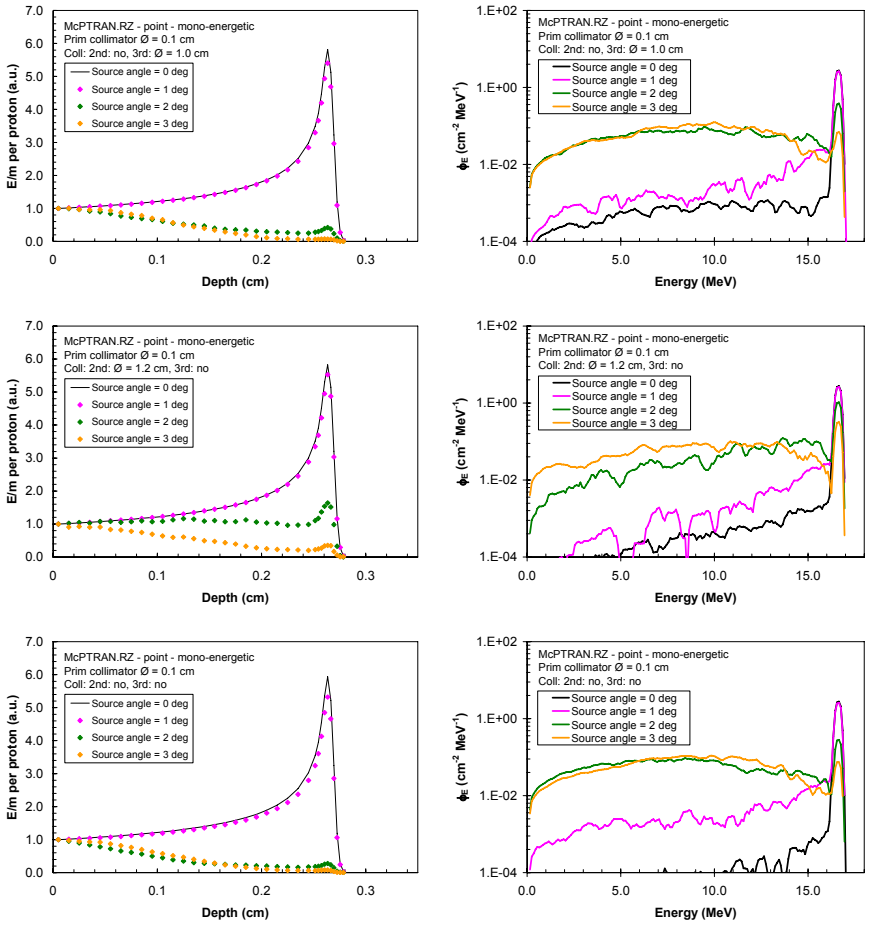

Figure 21. Left: depth dose profiles for the 1 mm diameter primary collimator in absence of either the secondary collimator, the third collimator or both the second and third collimators and for source angles ranging from 0 to 3 degrees. Right: corresponding proton spectra calculated at the surface of the phantom.

The simulations in absence of either one or both of the secondary and third collimators are shown in figure 21. This shows that the absence of the secondary collimator result only in a deterioration of the situation, which is, as can be seen from the spectra in figure 21, due to an increased amount of low-energy proton scatter reaching the phantom.

This has also the implication that using the quadrupole magnets as a means of forcing more of the beam through the secondary collimator might have a similar effect. On the other hand the beam optics system combined with the secondary collimator could possibly also serve as an energy selection tool but this should be investigated by detailed beam optics transport

based on the field characteristics of the proton beam transmitted through the primary collimator. The third collimator has little influence on the beam quality.

3.2. Experimental results

3.2.1. Intensity and stability of the beam

The beam intensity was reduced more than anticipated to dose rates of 2 to 12 Gy per minute at the phantom surface. This range is good for dosimetry, although for the alanine irradiations a dose rate of one order of magnitude higher would be ideal.

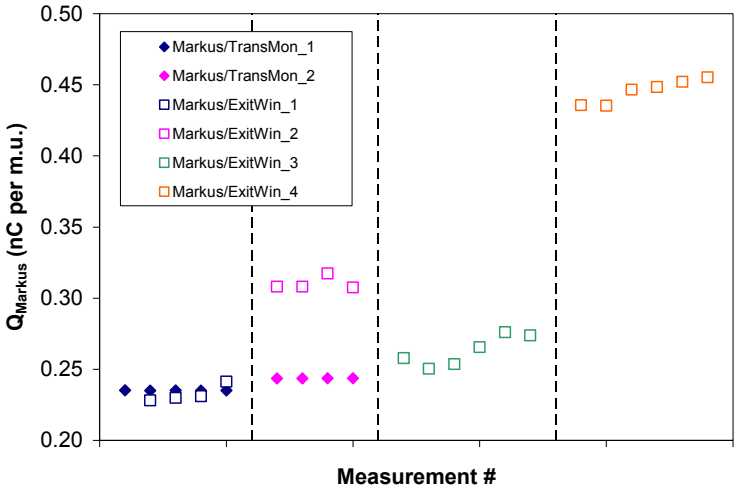

Figure 22. Ratio of the charge collected by the Markus chamber and the monitor signal, which was either the charge collected on the exit window or the charge collected by the transmission ionization chamber. The vertical lines indicate where beam tuning was performed.

A number of test runs were performed with the transmission chamber present and the Markus chamber positioned with its entrance window aligned with the surface of the phantom and with its sensitive volume in the centre of the proton field. The results in figure 22 show that for each run the statistical uncertainties of ratio of the ionization chamber to monitor signal is good but that the ratio is strongly dependent on the beam parameters as they change after beam tuning. The latter effect is worse when using the charge collected on the exit window as monitor. This indicates that changes in lateral beam uniformity might be the cause of these variations, given that the transmission chamber is on the same side of the collimator as the Markus, whereas the exit window is at the opposite side. The large variation of the charge measured on the exit foil might also indicate that there is a dependence on the current.

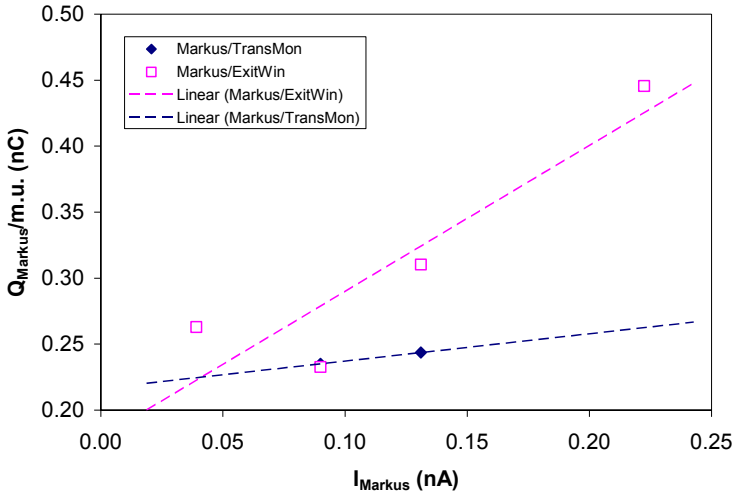

Figure 23. Charge collected by the Markus chamber per monitor unit plotted as a function of the approximate current measured by the Markus to evaluate the current dependence of the monitor signals.

Figure 23 gives an idea how much the monitor signal depends on the current measured by the Markus chamber. Within on set of measurements (between beam tuning) the standard deviations on the Markus to transmission monitor ratio was below 0.05% whereas on the Markus to exit window ratio was typically between 2% and 3%.

3.2.2. Film measurements of profiles

The film exposure images as well as the horizontal and vertical profiles through the centre are shown in figure 24. Each row shows from left to right the exposed film, the horizontal profile and the vertical profile. The images are 255x255 pixels in size and are all represented from a beam's eye view. The profiles are an average over a strip of 30 pixels wide in the centre of the film. A baseline was subtracted for the intensity in the parts outside the field. The profiles obtained with both film types agree in general well. The noise on the RTQA film is in general worse than for the EBT film which is possibly due to a lower sensitivity of the digital camera for the colouring of the RTQA film. The upper and middle sets (a) and (b) in figure 24 were obtained respectively at the surface of the phantom and at the exit window and were exposed shortly after one another without tuning. The lower set (c) was obtained after significant tuning of the beam.

It can be seen in figure 24 that the RTQA film suffers more from scratches, which show up as dips in the lateral profiles. It is also obvious that the beam profile has changed due to this re-tuning of the beam. In the subsequent irradiations of alanine stacks in the phantoms, it was decided to perform as little tuning as possible between and during irradiations by leaving the current on the magnets and the positioning of the extraction foil untouched while entering the accelerator room.

A few of the profiles with the RTQA films were also scanned at the Royal Marsden Hospital according to their normal clinical procedures. These are shown as grey lines in figure 24 and although the agreement is not perfect it is in general acceptable given the difference in the line width, possible differences in the actual line of the scan and some of the artefacts. This demonstrates the validity of our procedure with the digitised camera image.

(a)

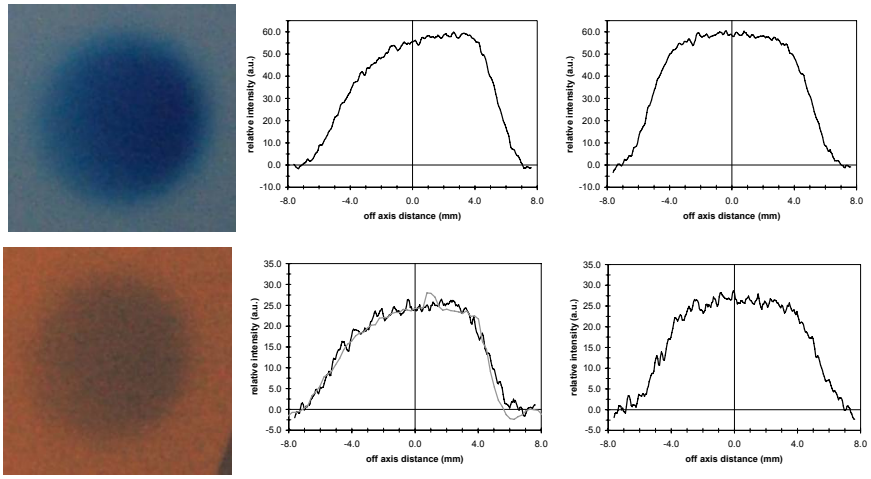

(b)

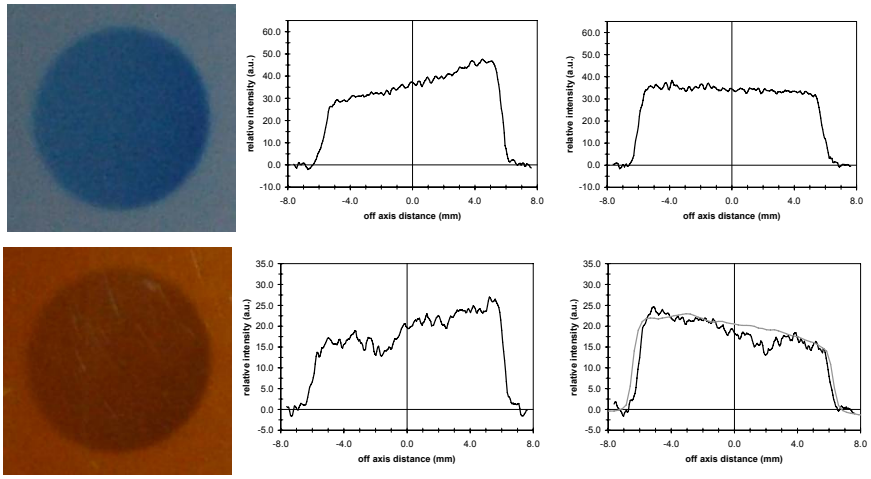

(c)

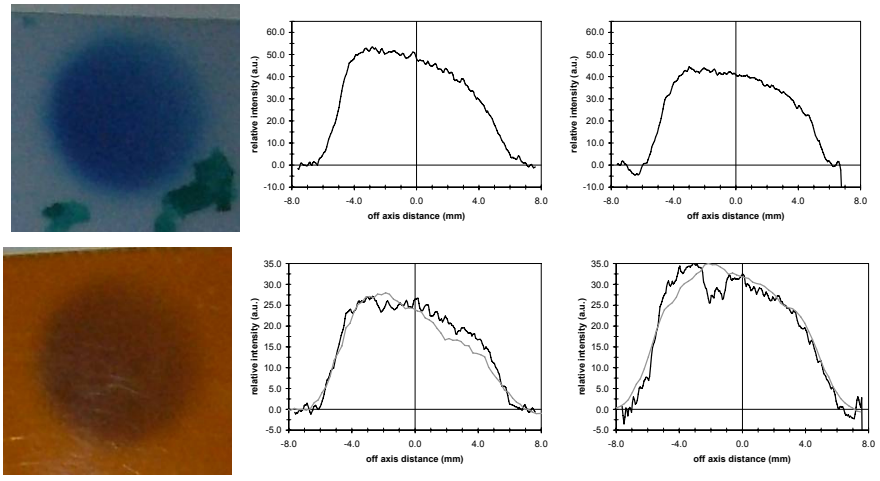

Figure 24. Lateral exposure images and horizontal and vertical profiles using two types of GafChromic film (see text for more details). The grey lines were measured at RMH.

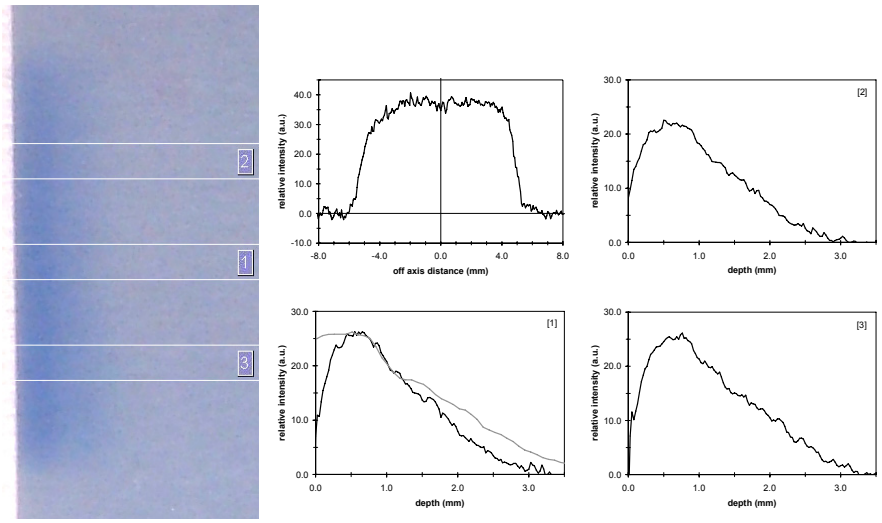

Figure 25. Left: exposure image with indication of the regions along which depth response curves were evaluated. Upper figure in the middle: lateral profile along the dose maximum. Other figures: depth response distributions with numbers corresponding to those indicated in the exposure image. The grey line was measured at RMH.

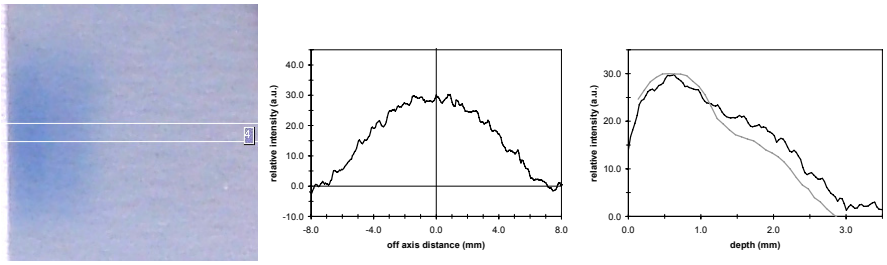

Figure 26. Left: exposure image with indication of the region along which the depth response curves was evaluated. Middle: lateral profile along the dose maximum. Right: depth response distribution. The grey line was measured at RMH.

Figures 25 and 26 show the exposure images and profiles for the only two pieces of radiochromic film in the set-up of figure 10 that were hit by the beam. In both pieces of films an artefact is visible on the left hand side corresponding to the edge of the film due to cutting. The piece of film shown in figure 25 was more or less centred on the beam axis, resulting in a lateral profile similar to the ones shown in figure 24. The piece of film in figure 26 was at the periphery of the beam profile and consequently the resulting lateral profile is distorted by the cylindrical edge of the beam.

Again, the depth dose profiles were scanned at the Royal Marsden Hospital as well according to their normal clinical procedures. Although also here there are some substantial differences that could be attributed to differences in the actual line and line width of the scan. Given that the discussion of the alanine results below is rather qualitative this was found to be acceptable.

The depth dose curves were surprising (the Monte Carlo results of section 3.1.5 were in fact obtained after these measurements) since they do not look like a Bragg peak at first sight. However, the maximum in the signal is possibly the actual Bragg peak which is smeared out by the presence of a substantial component of low-energy protons. There is a slight concern that the GafChromic film does not have a flat response as a function of energy but several papers (Vatnitsky 1997, Daftari et al. 1999 and Piermattei et al. 2000) shown that this effect is not very large and an explanation for the absence of the Bragg peak cannot be found there. In addition, there is some uncertainty about the exact profile near the surface given the artefact of the cutting edge, which could to some extent also contribute to the signal build-up effect. It was visually estimated on the exposure images where the surface was, but some sensitivity analysis on the choice of the surface position was done by shifting the curve in the comparison with the alanine measurements discussed in the next section.

An additional concern regarding the profile measurements using radiochromic film is the non-linearity of its dose response (all the data shown above assume a linear relation between dose and optical density). Figure 27 summarizes a number of calibration curves extracted from the literature. The quantity on the horizontal axis (*netOD*) is the optical density of the irradiated film minus the optical density of the unirradiated film. The symbols represent measured data and the curves are fits of the format $D = b \cdot netOD + c \cdot (netOD)^n$ (Devic et al. 2005) where $n = 2.5$ (except for the data of Todorovic et al 2006 where $n = 6$) and b and c are free parameters. The wide variety of different optical densities for the same dose level is explained by the diversity of light sources and scanning systems that were used. In order to give an idea of the potential non-linearity in the region of interest for our measurements, the graph on the right hand side of figure 27 presents the same data with normalised optical densities at 2 Gy. It is obvious that in this region the curves vary from almost linear to substantially curved leading to maximum dose over-predictions of about 20% if a linear calibration curve would be used. Since at present we do not have sufficient information for establishing a calibration curve for our read-out procedure, we have investigated the two extreme cases in the comparison with the alanine dosimeters in the next section. To this end, a non-linearity correction based on the most extreme curve in figure 27b was applied to the depth dose curves of figure 25.

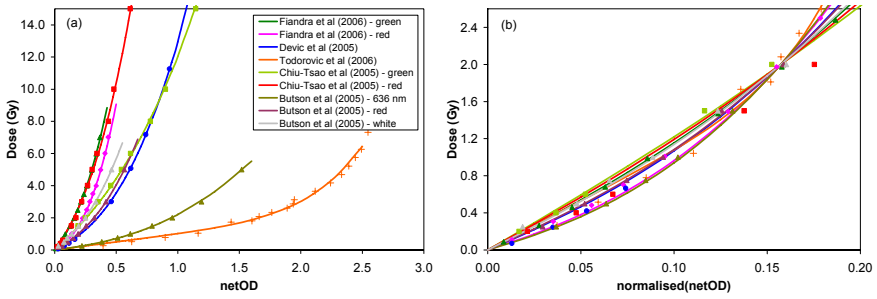

Figure 27. Left: Dose versus optical density calibration curves for a number of EBT/scan systems reported in the literature. Right: normalised curves to give equal optical density at 2 Gy.

3.2.3. Alanine irradiations

Figure 28 compares the response measured with the three stacks of alanine pellets with what would be expected from the film measurements. To this end the film measurements were integrated over a depth equivalent to the estimated thickness (0.056 g cm^{-2}) of the pellets. For figures 28a, 28b and 28c the signals for the first pellet from the phantom surface were

normalised to unity. The response curve of the film was also normalised so as to give unity for the first estimated pellet dose. This was done for all the depth dose curves shown in figures 25 and 26, resulting in quantitative differences, but all qualitative aspects are similar as in the results obtained with curve [1] indicated in figure 25. It is clear that there is a substantial dependence on the choice of the position of the surface making it very difficult to make an absolute comparison. In addition, the non-linearity of the radiochromic film response has a substantial effect, making a numerical interpretation comparison difficult to interpret.

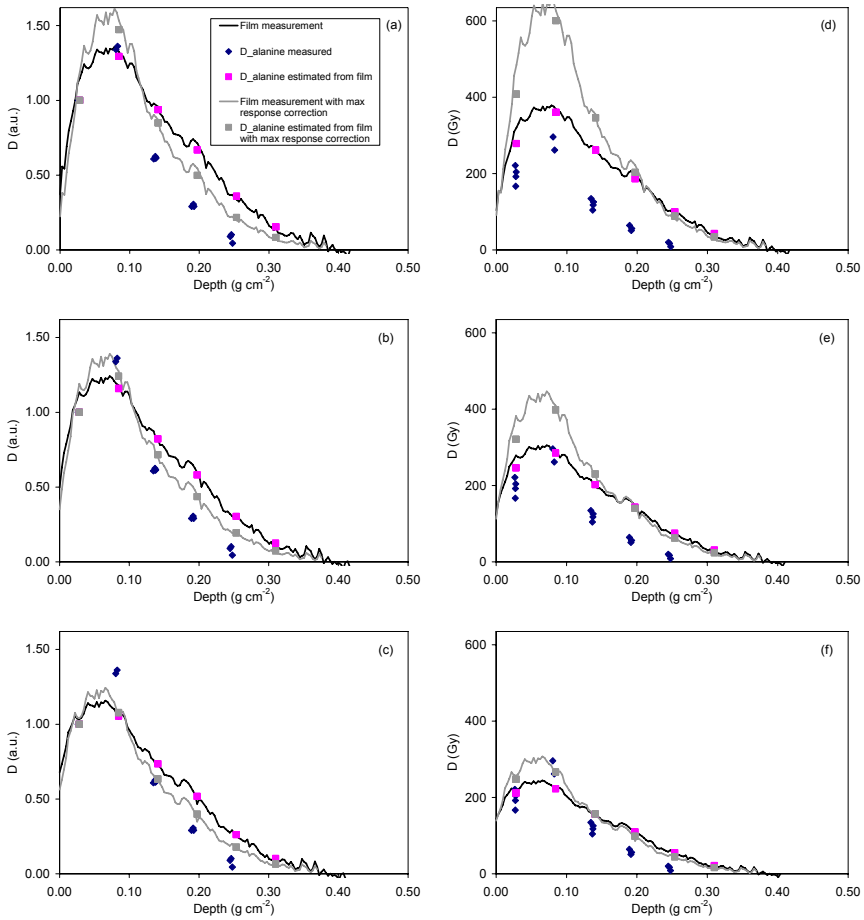

Figure 28. (a), (b) and (c): relative response of stacks of alanine dosimeters compared with film measurements (black based on a linear response, grey based on the most extreme curved response in figure 27) obtained using the depth profile indicated with [1], shifted over respectively 0.00 mm, 0.05 mm and 0.10 mm. (d), (e) and (f): the same three graphs in terms of absolute dose (see text).

It is clear that the alanine pellets confirm the shape of the depth profile from the film measurements. Both the pellets and the film show a signal build-up from the surface followed by an attenuation-like curve, but the depth profile seems to fall off more quickly as a function of depth for the alanine pellets. This could be an indication of a lower response of alanine to low-energy protons than the radiochromic film but at this stage we can not exclude another effect such as a contribution from neutrons or gammas given the very low proton fluence that arrives at the phantom.

When the curve is slightly shifted, to account for the possible error in the exact surface position, the fall-off curves come slightly closer, but the distinct maximum in the alanine pellets predicted by the film measurements disappears, suggesting that the choice of the surface is approximately right and the signal build-up is real and not an artefact due to the cutting edge.

Figures 28d, 28e and 28f show the same data but expressed in absolute dose. To this end, the film measurement was normalised such that the dose at a depth of 30 μm (the estimated window thickness of the Markus chamber) coincided with the dose measured at the phantom surface by the Markus chamber for the number of monitor units delivered to the alanine phantom. The large variation of the absolute dose resulting from the film measurements using only very small differences in surface position (within the level of the size of the cutting edge) illustrates once again the difficulty of making an absolute comparison. The variation in the alanine doses also illustrates the unreliability of the monitoring set-up since the same number of monitor units (charge collected at the exit window) was delivered for each stack. On the other hand it is promising that the relative depth doses are very consistent from stack to stack indicating that even though the beam profiles influence the phantom dose to monitor ratio substantially, the beam quality is not so sensitive to those changes.

Dose to water obtained with the Markus chamber in the set-up of figure 9 was found to be 82 Gy, whereas the dose that would be derived from the pellets (using the relative depth dependence from the measurements in figure 28) was found to be 93 Gy, both relative to the first and the third pellet (the second one broke). The difference of more than 11% is possibly due to a lateral non-equilibrium perturbation caused by the PMMA holder of the pellets. This could be simulated by Monte Carlo, but could also be avoided by choosing a PMMA holder thickness equal to the combined thickness of the pellets that are being calibrated.

4. CONCLUSIONS

The experiments demonstrated that a stable beam of sufficiently low intensity for dosimetry can be produced at the Biont 18 MeV proton beam. Monte Carlo simulations suggest that the beam was heavily contaminated with low-energy protons due to an oblique incidence of the primary beam through the pinhole-sieve primary collimator. Provided this can be improved by using the 1 mm diameter collimator and by keeping the beam steering consistently straight through the collimator, the present beam allows to perform accurate relative measurements using a stack of alanine pellets and accurate absolute calibration of one or more alanine pellets by directly placing them in front of a Markus chamber. In order to use a monitoring system enabling a calibration with the substitution method the stability steering of the beam through the primary collimator should also be improved in order to keep the beam profiles constant. Biont investigates the possibility of installing a lateral beam monitoring system before the primary collimator to stabilise the steering by a feedback system to one of the beam tuning parameters (cyclotron magnetic field, extraction foil position, horizontal and vertical steering magnets).

A substantial set of Monte Carlo simulations was done to support the design of the beam set-up as well as in the interpretation of the experimental data. The codes SRIM, MCNPX and two versions of McPTRAN are in good agreement in the conditions that can be simulated by all or two of them. This indicates that whichever of them can be used to calculate particular problems for which one of the codes is more suited, e.g. MCNPX is more suited for calculations of secondary neutrons and gammas, whereas SRIM is more suited for combining with beam optics programs such as S^3M (Pavlovič and Strašík, 2006).

The main remaining obstacle for a successful comparison between alanine and the ionization chamber are the spectral characteristic of the beam, which need to be improved by a better control of the steering as discussed above. The Monte Carlo simulations suggest that the oblique incidence of the beam through primary collimator is the main cause of the large low-energy proton component but also that the spectral characterises can be improved by a combination of increasing the size of the primary collimator hole and increasing the thickness of the primary scatter foil.

5. ACKNOWLEDGEMENTS

This work was funded as part of the UK National Measurement System, Ionising Radiation Metrology Programme and the UK National Measurement Secondment Scheme by the National Measurement System Policy Unit of the UK Department for Innovation, Universities and Skills.

6. REFERENCES

ANDREO, P., BURNS, D.T., HOHLFELD, K., HUQ, M.S., KANAI, T., LAITANO, F., SMYTH, V.G. and VYNCKIER, S. Absorbed dose determination in external beam radiotherapy: an international code of practice for dosimetry based on standards of absorbed dose to water. *IAEA Technical Report Series 398*, Vienna, IAEA, 2000.

BARTOLOTTA, A., TONGHI, L. B., BRAI, M., CUTTONE, G., FATTIBENE, P., ONORI, S., RAFFAELE, L., ROVELLI, A., SABINI, M.G. and TERI, G. Response characteristics of thermoluminescence and alanine-based dosemeters to 16 and 25 MeV proton beams. *Radiat. Prot. Dosim.*, **85**, 353-356, 1999.

BASSLER, N. Experimental studies relevant for antiproton cancer therapy. *PhD thesis*, University of Aarhus, Denmark, 2006.

BERGER, M.J. Proton Monte Carlo transport program PTRAN *National Institute for Standards and Technology Report NISTIR 5113*, NIST, Gaithersburg, USA ,1993.

BRADSHAW, W.W., CADENA JR., D.G., CRAWFORD, G.W. and SPETZLER, H.A.W. The use of alanine as a solid dosimeter. *Radiat. Res.*, **17**, 11-21, 1962.

BUTSON, M.J., CHEUNG, T., and YU, P.K.N. Absorption spectra variations of EBT radiochromic film from radiation exposure. *Phys. Med. Biol.*, **50**, N135-N140, 2005.

CHIU-TSAO, S.-T., HO, Y., SHANKAR, R., WANG, L., and HARRISON, L.B. Energy dependence of response of new high sensitivity radiochromic films for megavoltage and kilovoltage radiation energies. *Med. Phys.*, **32**, 3350-3354, 2005.

CUTTONE, G., RAFFAELE, L., TONGHI, L., ROVELLI, A., SABINI, M. G., EGGER, E., KACPEREK, A., BRAI, M., BARTOLOTTA, A., TERI, G., ONORI, S. and FATTIBENE, P. First dosimetry intercomparison results for the CATANA project. *Phys. Medica*, **15**, 121-130, 1999.

DAFTARI, I., CASTENADAS, C., PETTI, P.L., SINGH, R.P. and VERHEY, L.J. An application of GafChromic MD-55 film for 67.5 MeV clinical proton beam dosimetry. *Phys. Med. Biol.*, **44**, 2735-2745, 1999.

DEVIC, S., SEUNTJENS, J., SHAM, E., PODGORSAK, E.B., ROSS SCHMIDTLEIN, C., KIROV, A.S., and SOARES, C.G. Precise radiochromic film dosimetry using a flat-bed document scanner. *Med. Phys.*, **32**, 2245-2253, 2005.

EBERT, P.J., HARDY, K.A. and CADENA, D.G. Energy dependence of free radical production in alanine. *Radiat. Res.*, **26**, 178-197, 1965.

FATTIBENE, P., CALICCHIA, A., D'ERRICO, F., DEANGELIS, C., EGGER, E. and ONORI, S. Preliminary assessment of LiF and alanine detectors for the dosimetry of proton therapy beams. *Radiat. Prot. Dosim.*, **66**, 305-309, 1996.

FATTIBENE, P., DE ANGELI,S C., ONORI, S. and CHERUBINI, R. Alanine response to proton beams in the 1.6-6.1 MeV energy range *Radiat. Prot. Dosim.*, **101**, 465-468, 2002.

FIANDRA, C., RICARDI, U., RAGONA, R., ANGLESIO, S., GIGLIOLI, F.R., CALAMIA, E., and LUCIO, F. Clinical use of EBT model Gafchromic^{TM} film in radiotherapy *Med. Phys.*, **33**, 4314-4319, 2006.

GALL, K., DESROSIERS, M., BENSEN, D. and SERAGO, C. Alanine EPR dosimeter response in proton therapy beams. *Appl. Radiat. Isot.*, **47**, 1197-1199, 1996.

HANSEN, J.W. and OLSEN, K.J. Theoretical and experimental radiation effectiveness of the free radical dosimeter alanine to irradiation with heavy charged particles. *Radiat. Res.*, **104**, 15-27, 1985.

ICRU. Stopping powers and ranges for electrons and positrons. *International Commission on Radiation Units and Measurements Report 37*, Bethesda USA, ICRU, 1984.

ICRU. Stopping powers and ranges for protons and alpha particles. *International Commission on Radiation Units and Measurements Report 49*, Bethesda USA, ICRU, 1993.

ICRU. Nuclear data for neutron and proton radiotherapy and for radiation protection dose. *International Commission on Radiation Units and Measurements Report 63*, Bethesda USA, ICRU, 2000.

NICHIPOROV, D., KOSTJUCHENKO, V., PUHL, J.M., BENSEN, D.L., DESROSIERS, M.F., DICK, C.E., MCLAUGHLIN, W.L., KOJIMA, T., COURSEY, B.M. and ZINK, S. Investigation of applicability of alanine, and radiochromic detectors to dosimetry of proton clinical beams. *Appl. Radiat. Isot.*, **46**, 1355-1362, 1995.

OLSEN, K.J. and HANSEN, J.W. The response of the alanine dosemeter to low energy protons and high energy heavy charged particles. *Radiat. Prot. Dosim.*, **31**, 81–84, 1990.

ONORI, S., D'ERRICO, F., DEANGELIS, C., EGGER, E., FATTIBENE, P. and JANOVSKY, I. Proton response of alanine based pellets and films. *Appl. Radiat. Isot.*, **47**, 1201-1204, 1996.

ONORI, S., D'ERRICO, F., DE-ANGELIS, C., EGGER, E., FATTIBENE, P. and JANOVSKY, I. Alanine dosimetry of proton therapy beams. *Med. Phys.*, **24**, 447-453, 1997.

PALMANS, H. Effect of alanine energy response and phantom material on depth dose measurements in ocular proton beams. *Technol. Cancer Res. Treat.*, **2**, 579-86, 2003.

PALMANS, H. McPTRAN.CAVITY and McPTRAN.RZ, Monte Carlo codes for the simulation of proton beams and calculation of proton detector perturbation factors. *In: The*

Monte Carlo Method: Versatility Unbounded in a Dynamic Computing World (Illinois, USA: American Nuclear Society), 2005

PALMANS, H., THOMAS, R., SHIPLEY, D. and KACPEREK, A. Light-ion beam dosimetry. *NPL report DQL-RD003*, 2006

PAVLOVIČ, M. and STRAŠÍK, I. Supporting routines to the SRIM-code. *Nucl. Instr. Meth. B*, submitted, 2006

PIERMATTEI, A., MICELI, R., AZARIO, L., FIDANZIO, A., DELLE CANNE, S., DE ANGELIS, C., ONORI, S., PACILIO, M., PETETTI, E., RAFFAELE, L. and SABINI, M.G. Radiochromic film dosimetry of a low energy proton beam. *Med. Phys.*, **27**, 1655-1660, 2000.

SHARPE, P.H., RAJENDRAN, K. and SEPHTON, J.P. Progress towards an alanine/ESR therapy level reference dosimetry service at NPL. *Appl. Radiat. Isot.*, **47**, 171-1175, 1996.

SHARPE, P.H. and SEPHTON, J.P. An automated system for the measurement of alanine/EPR dosimeters. *Appl. Radiat. Isot.*, **52**, 1185-1188, 2000.

TODOROVIC, M., FISCHER, M., CREMERS, F., THOM, E., and SCHMIDT, R. Evaluation of GafChromic EBT prototype B for external beam dose verification. *Med. Phys.*, **33**, 1321-1328, 2006.

VATNITSKY, S.M. Radiochromic film dosimetry for clinical proton beams. *Appl. Radiat. Isot.*, **48**, 643-51, 1997.

WALIGORSKI, M.P. R., DANIALY, G., LOH, K.S. and KATZ, R. The response of the alanine detector after charged-particle and neutron irradiations. *Appl. Radiat. Isot*., **40**, 923-933, 1989.

WATERS, L.S. MCNPX-User's Manual Version 2.4.0. Los Alamos National Laboratory, Los Alamos, NM, USA, 2002.

ZIEGLER, J.F. and BIERSACK, J.P. SRIM 2003. http://www.SRIM.org, 2003.